

Preparation of Single-Layer $\text{MoS}_{2x}\text{Se}_{2(1-x)}$ and $\text{Mo}_x\text{W}_{1-x}\text{S}_2$ Nanosheets with High-Concentration Metallic 1T Phase

Chaoliang Tan, Wei Zhao, Apoorva Chaturvedi, Zhen Fei, Zhiyuan Zeng, Junze Chen, Ying Huang, Peter Ercius, Zhimin Luo, Xiaoying Qi, Bo Chen, Zhuangchai Lai, Bing Li, Xiao Zhang, Jian Yang, Yun Zong, Chuanhong Jin, Haimei Zheng, Christian Kloc,* and Hua Zhang*

Single- and few-layer transition metal dichalcogenide (TMD) nanosheets, such as MoS_2 , WS_2 , MoSe_2 , etc., have attracted increasing attention in the past few years due to their unique chemical and electronic properties^[1–5] as well as various promising applications in electronic/optoelectronic devices,^[6,7] electrocatalysis,^[8,9] sensors,^[10–12] energy storage,^[13,14] and biomedicine.^[15,16] Ultrathin 2D ternary TMD nanosheets, such as $\text{MoS}_{2x}\text{Se}_{2(1-x)}$ and $\text{Mo}_x\text{W}_{1-x}\text{S}_2$, are also receiving much attention.^[17–25] The ternary structure of ultrathin 2D TMD nanosheets enables them with some appealing properties or functions, such as tunable band gaps^[18–22] and enhanced catalytic activity for hydrogen generation.^[23,25] Currently, single- or few-layer ternary TMD nanosheets, such as $\text{MoS}_{2x}\text{Se}_{2(1-x)}$

and $\text{Mo}_x\text{W}_{1-x}\text{S}_2$, are normally prepared by mechanical exfoliation^[17,18] and chemical vapor deposition.^[19–22] However, few-layer ternary TMD flakes can be prepared by sonication-assisted exfoliation^[23,24] and wet-chemical synthesis methods.^[25] Therefore, it still remains a big challenge for the high-yield and large-scale preparation of single-layer ternary TMD nanosheets in solution.

Generally, ultrathin 2D TMD nanosheets have a 2H crystal phase (for example, MoS_2 , WS_2 , and MoSe_2), rendering them semiconducting properties with large band gaps of 1–2 eV and thus appealing for electronics/optoelectronics.^[1,2] However, their low intrinsic electrical conductivity limited their potentials for some specific applications, such as electrodes for electrocatalysis and electrochemical supercapacitors, and low-resistance contact transistors.^[1,2] Recently, it has been demonstrated that the phase engineering of ultrathin 2D TMD nanosheets from semiconducting 2H phase to metallic 1T phase is an effective approach to improve the conductivity of TMD nanosheets^[26] and thus to achieve much enhanced performance in electrocatalytic hydrogen evolution,^[27–29] electrochemical supercapacitors,^[30] and low-resistance contact transistors.^[31,32] Normally, the phase engineering of 2D TMD nanosheets can be achieved by the Li-intercalation with *n*-butyllithium,^[27,28,30,31,33] laser irradiation,^[32] electron beam irradiation,^[34] and gate-controlled Li-intercalation.^[35] Recently, the metallic 1T TMD nanosheets (for example, WS_2) can also be directly synthesized by the wet-chemical method.^[36] Here, we use our recently developed electrochemical Li-intercalation and exfoliation method^[37] to prepare the high-yield and scalable production of single-layer ternary TMD nanosheets with high-concentration metallic 1T phase ($\approx 66\%$), including $\text{MoS}_{2x}\text{Se}_{2(1-x)}$ and $\text{Mo}_x\text{W}_{1-x}\text{S}_2$, from their 2H-phase layered bulk crystals (**Scheme 1**). As a proof-of-concept application, a thin film of the exfoliated $\text{MoS}_{2x}\text{Se}_{2(1-x)}$ nanosheets with high concentration of metallic 1T phase is coated on a fluorine-doped tin oxide (FTO) substrate by simple drop-coating method, which is then used as an efficient electrocatalyst on counter electrode (CE) for the tri-iodide reduction in a dye-sensitized solar cell (DSSC).

Micrometer-sized 2H-phase layered bulk crystals of $\text{MoS}_{2x}\text{Se}_{2(1-x)}$ and $\text{Mo}_x\text{W}_{1-x}\text{S}_2$ were synthesized from their elementary powders via the chemical vapor transport method (see the Experimental Section in the Supporting Information

C. L. Tan, Dr. W. Zhao, A. Chaturvedi, J. Z. Chen, Y. Huang, Dr. Z. M. Luo, B. Chen, Z. C. Lai, X. Zhang, J. Yang, Prof. C. Kloc, Prof. H. Zhang
Center for Programmable Materials
School of Materials Science and Engineering
Nanyang Technological University
50 Nanyang Avenue, Singapore 639798, Singapore
E-mail: CKloc@ntu.edu.sg; hzhang@ntu.edu.sg



Z. Fei, Prof. C. H. Jin
State Key Laboratory of Silicon Materials
School of Materials Science and Engineering
Zhejiang University
Hangzhou, Zhejiang 310027, China

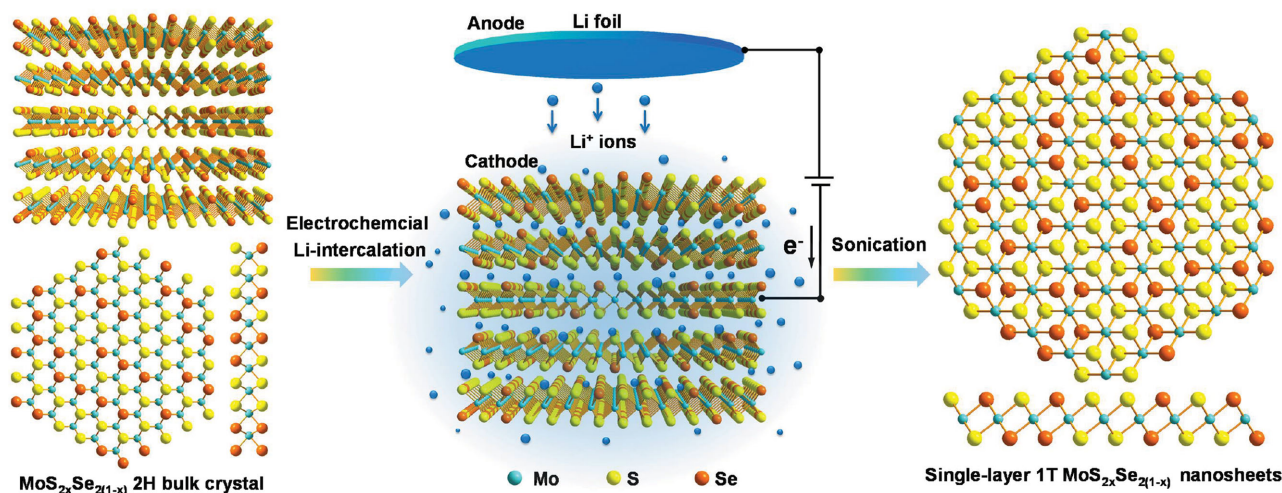
Dr. Z. Y. Zeng, Dr. H. M. Zheng
Materials Sciences Division
Lawrence Berkeley National Laboratory
Berkeley, CA 94720, USA

Dr. P. Ercius
National Center for Electron Microscopy
Molecular Foundry
Lawrence Berkeley National Laboratory
Berkeley, CA 94720, USA

Dr. X. Y. Qi
Singapore Institute of Manufacturing Technology
71 Nanyang Drive, Singapore 638075, Singapore

Dr. B. Li, Dr. Y. Zong
Institute of Materials Research and Engineering (IMRE)
A*STAR (Agency for Science Technology and Research)
2 Fusionopolis Way, Innovis #08-03, Singapore 138634, Singapore

DOI: 10.1002/sml.201600014



Scheme 1. Schematic illustration of preparation of single-layer ternary TMD nanosheets with high-concentration metallic 1T phase from their 2H-phase layered bulk crystals by using the electrochemical Li-intercalation and the exfoliation method. Note that $\text{MoS}_{2x}\text{Se}_{2(1-x)}$ is used as an example in this scheme.

for details) (Figures S1 and S2, Supporting Information). Based on the energy-dispersive X-ray spectroscopy (EDS) analyses (Figures S1c and S2c, Supporting Information), the chemical formulae of $\text{MoS}_{2x}\text{Se}_{2(1-x)}$ and $\text{Mo}_x\text{W}_{1-x}\text{S}_2$ crystals are determined to be $\text{MoS}_{1.35}\text{Se}_{0.65}$ and $\text{Mo}_{0.65}\text{W}_{0.35}\text{S}_2$, respectively. The as-prepared bulk crystals were then used as the sources to produce single-layer ternary nanosheets by using our recently developed electrochemical Li-intercalation and exfoliation method (see the Experimental Section in the Supporting Information for details, Scheme 1).^[37] The size and thickness of exfoliated $\text{MoS}_{2x}\text{Se}_{2(1-x)}$ nanosheet are 0.1–2 μm (Figure 1a–c) and 1.1–1.2 nm (Figure 1b and Figure S3, Supporting Information), respectively, suggesting its single-layer nature. The obtained $\text{MoS}_{2x}\text{Se}_{2(1-x)}$ nanosheet can be well-dispersed in water to form a stable colloidal suspension (inset in Figure 1a). The selected area electron diffraction (SAED) pattern of a typical $\text{MoS}_{2x}\text{Se}_{2(1-x)}$ nanosheet (Figure 1d) shows bright diffraction spots with sixfold symmetry (Figure 1e). The outer and inner six spots can be indexed to the (110) and (100) planes of $\text{MoS}_{2x}\text{Se}_{2(1-x)}$, respectively. The high-resolution transmission electron microscope (HRTEM) image gives continuous lattice fringes with lattice distance of 0.276 nm (Figure 1f), assignable to the (100) planes of $\text{MoS}_{2x}\text{Se}_{2(1-x)}$ crystal. The signals of Mo, S, and Se can be observed in its EDS spectrum (Figure S4, Supporting Information) and their homogeneous distribution in the nanosheet is clearly evidenced by the elemental mapping (Figure 1g).

The S and Se atoms in the $\text{MoS}_{2x}\text{Se}_{2(1-x)}$ nanosheet can be observed in the high-angle annular dark-field image obtained by using an aberration-corrected scanning transmission electron microscope (STEM). Figure 2a clearly shows the triangular arrangement of Mo atoms, indicating the 1T phase structure of $\text{MoS}_{2x}\text{Se}_{2(1-x)}$ nanosheet.^[26,30,31] Since the atom image intensity is directly related to the Z number of the atoms, the Se atom gives a brighter contrast than does the S atom due to its larger Z number.^[19] The STEM image of $\text{MoS}_{2x}\text{Se}_{2(1-x)}$ nanosheet shows that the Se atoms randomly occupied the S sites in the single-layer ternary nanosheet,

while the S atoms cannot be distinguished because they show negligible contrast in the STEM image of 1T-phase $\text{MoS}_{2x}\text{Se}_{2(1-x)}$ due to the smaller Z number of S atom (Figure 2a and Figure S5, Supporting Information).

Furthermore, the presence of high-concentration metallic 1T crystal phase in the exfoliated $\text{MoS}_{2x}\text{Se}_{2(1-x)}$ nanosheets was confirmed by X-ray photoelectron spectroscopy (XPS), Raman spectroscopy, and UV–vis absorption spectroscopy. In order to quantitatively calculate the concentration of 1T phase, XPS was used to study the phase compositions in the bulk crystal of $\text{MoS}_{2x}\text{Se}_{2(1-x)}$, and the exfoliated nanosheets of $\text{MoS}_{2x}\text{Se}_{2(1-x)}$ before and after annealing at 300 °C under Ar (Figure 2b,c and Figure S6, Supporting Information). The Mo 3d spectrum of bulk crystal gives peaks at around 229.0 and 232.1 eV (Figure 2b), assignable to $\text{Mo}^{4+} 3d_{5/2}$ and $\text{Mo}^{4+} 3d_{3/2}$ of 2H-phase $\text{MoS}_{2x}\text{Se}_{2(1-x)}$, respectively.^[38,39] The deconvolution of Mo 3d spectrum of exfoliated nanosheets indicates that the two main peaks shifted to lower binding energy by ≈ 0.8 eV (228.2 and 231.3 eV) with respect to the position of 2H $\text{MoS}_{2x}\text{Se}_{2(1-x)}$ peaks (229.0 and 232.1 eV) (Figure 2b). Moreover, the additional peaks at 161.2 and 162.4 eV (or 53.5 and 54.5 eV) appeared besides the known peaks of 2H phase $\text{MoS}_{2x}\text{Se}_{2(1-x)}$ at 161.9 and 163.1 eV (or 54.2 and 55.2 eV) in the S 2p (or Se 2d) spectra (Figure 2c and Figure S6, Supporting Information).^[39,40] All the analyses of XPS Mo 3d, S 2p, and Se 2d spectra prove the presence of 1T phase in the exfoliated $\text{MoS}_{2x}\text{Se}_{2(1-x)}$ nanosheets, which is similar to that of chemically exfoliated 1T MoS_2 nanosheets.^[33] The calculated concentration of 1T phase is as high as $\approx 66\%$ based on the Mo 3d spectrum (Figure 2b). Note that the 1T peaks can be totally quenched after the exfoliated $\text{MoS}_{2x}\text{Se}_{2(1-x)}$ nanosheets were annealed at 300 °C (Figure 2b,c and Figure S6, Supporting Information), suggesting the restoration of 2H phase from 1T phase.^[27,33] Raman spectroscopy was used to characterize the aforementioned three $\text{MoS}_{2x}\text{Se}_{2(1-x)}$ samples. Three prominent peaks corresponding to the 2H MoS_2 -like A_{1g} (402 cm^{-1}) and E'_{2g} (374 cm^{-1}) modes and the 2H MoSe_2 -like E'_{2g} (272 cm^{-1}) mode are clearly observed in three samples (Figure S7,

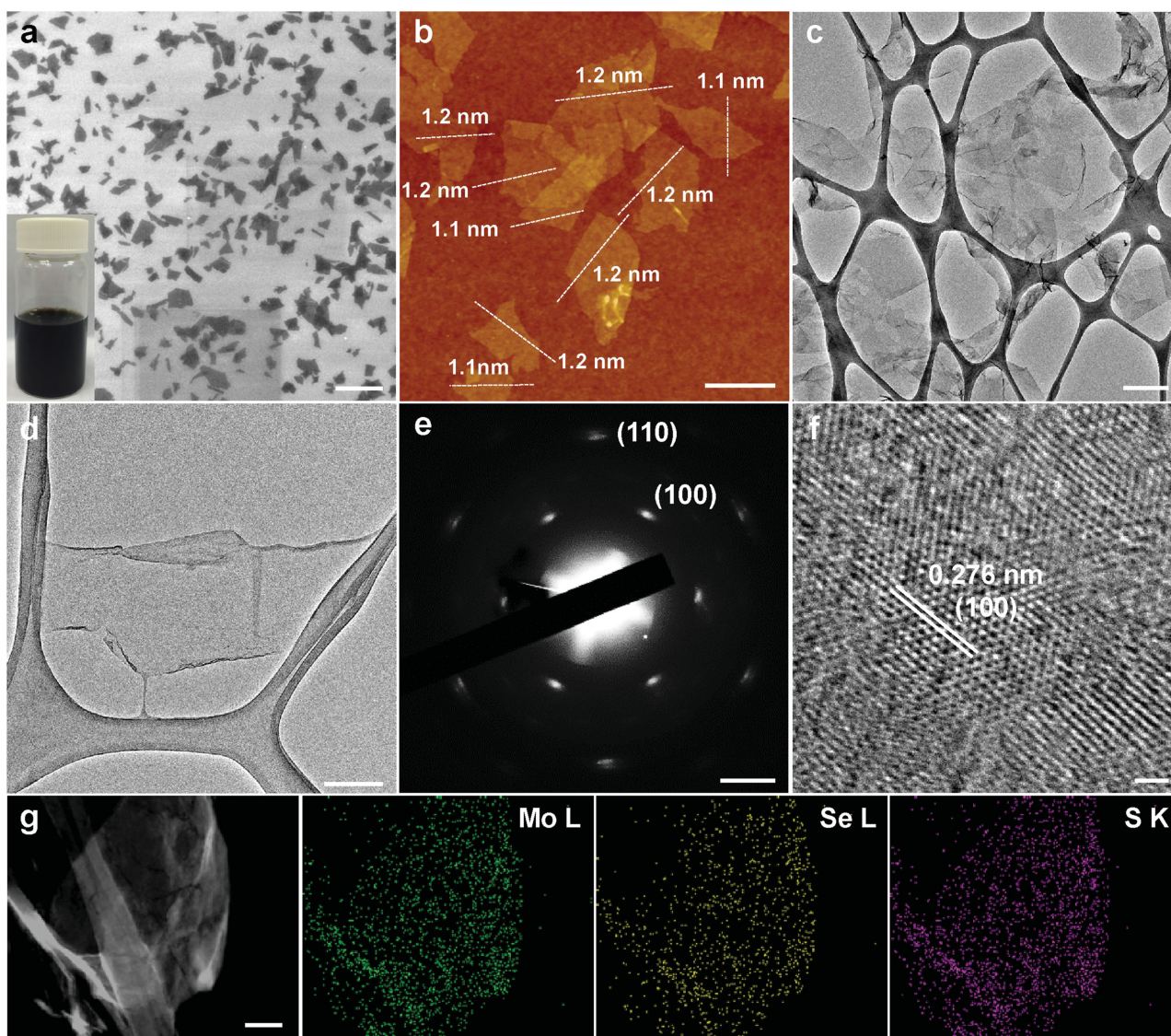


Figure 1. Characterization of $\text{MoS}_{2x}\text{Se}_{2(1-x)}$ nanosheets. a) SEM image and b) AFM height image of $\text{MoS}_{2x}\text{Se}_{2(1-x)}$ nanosheets (scale bars, a: 2 μm ; b: 500 nm). Inset in (a): photograph of colloidal suspension of $\text{MoS}_{2x}\text{Se}_{2(1-x)}$ nanosheets. c) TEM image of $\text{MoS}_{2x}\text{Se}_{2(1-x)}$ nanosheets (scale bar, 500 nm). d) TEM image of a typical $\text{MoS}_{2x}\text{Se}_{2(1-x)}$ nanosheet (scale bar, 200 nm). e) The corresponding SAED pattern of the $\text{MoS}_{2x}\text{Se}_{2(1-x)}$ nanosheet in (d) (scale bar, 2 $1/\text{nm}$). f) HRTEM image of a typical $\text{MoS}_{2x}\text{Se}_{2(1-x)}$ nanosheet (scale bar, 1 nm). g) EDS elemental mapping of a typical $\text{MoS}_{2x}\text{Se}_{2(1-x)}$ nanosheet (scale bar, 100 nm).

Supporting Information).^[40] Only the exfoliated $\text{MoS}_{2x}\text{Se}_{2(1-x)}$ nanosheet exhibits small peaks, around 140 and 300 cm^{-1} , in the lower frequency region (Figure S7, Supporting Information), corresponding to the distorted 1T phase Raman active modes, J_1 and J_3 , respectively, which are similar to the chemically exfoliated 1T MoS_2 nanosheets.^[33] The presence of 1T phase in exfoliated $\text{MoS}_{2x}\text{Se}_{2(1-x)}$ nanosheets was also evidenced by the absorption spectra (Figure 2d). No obvious characteristic peaks of 2H $\text{MoS}_{2x}\text{Se}_{2(1-x)}$ can be observed in the exfoliated $\text{MoS}_{2x}\text{Se}_{2(1-x)}$ nanosheet film, except a small peak at around 380 nm (Figure 2d). In contrast, after annealing of the exfoliated $\text{MoS}_{2x}\text{Se}_{2(1-x)}$ film at 300 $^\circ\text{C}$, the characteristic A and B excitonic peaks of 2H $\text{MoS}_{2x}\text{Se}_{2(1-x)}$ at 650 and 715 nm, respectively, and the convoluted C and D excitonic peaks at around 443 nm were clearly observed (Figure 2d), suggesting the restoration of 2H phase.^[33]

Similarly, the single-layer ternary $\text{Mo}_x\text{W}_{1-x}\text{S}_2$ nanosheets with high-concentration metallic 1T phase can also be prepared by exfoliation of its bulk crystal using the same method (Figure 3),^[37] and the stable colloidal suspension of $\text{Mo}_x\text{W}_{1-x}\text{S}_2$ nanosheets was obtained (inset in Figure 3a). The well-dispersed $\text{Mo}_x\text{W}_{1-x}\text{S}_2$ nanosheets with size similar to $\text{MoS}_{2x}\text{Se}_{2(1-x)}$ nanosheets were confirmed by the SEM, AFM, and low-magnification TEM images (Figure 3a–c). The typical thickness of $\text{Mo}_x\text{W}_{1-x}\text{S}_2$ nanosheets is 0.9–1.2 nm (Figure 3b and Figure S8, Supporting Information), proving their single-layer nature. The hexagonal diffraction spots can be observed from the SAED pattern of a typical $\text{Mo}_x\text{W}_{1-x}\text{S}_2$ nanosheet (Figure 3d,e). The outside and inner six spots at the SAED pattern are corresponding to the (110) and (100) planes of the $\text{Mo}_x\text{W}_{1-x}\text{S}_2$ nanosheet, respectively. The HRTEM image reveals the continuous lattice fringe with a lattice spacing

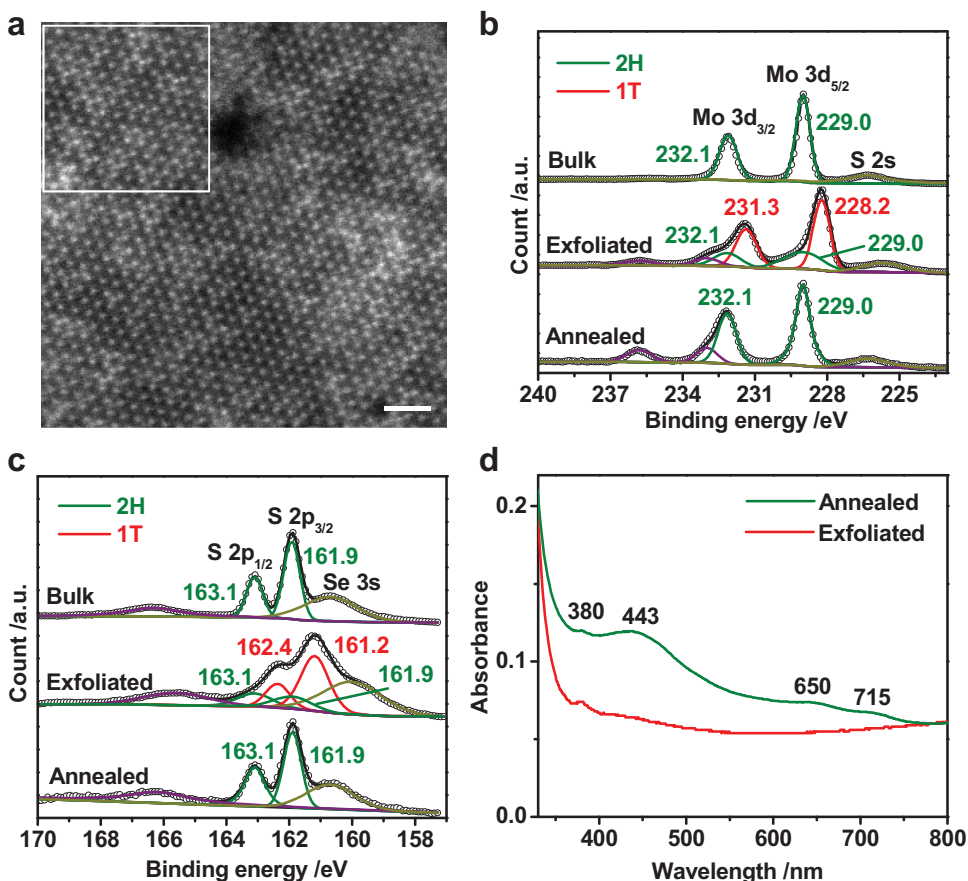


Figure 2. Characterization of the presence of 1T phase in the exfoliated $\text{MoS}_{2x}\text{Se}_{2(1-x)}$ nanosheets. a) Atomic STEM image of a typical exfoliated $\text{MoS}_{2x}\text{Se}_{2(1-x)}$ nanosheet (scale bar, 1 nm). Figure S5 (Supporting Information) gives individual Mo (light blue dot) and Se (orange dot) atoms in the white square in (a). b) High-resolution XPS Mo 3d spectrum of bulk crystal of $\text{MoS}_{2x}\text{Se}_{2(1-x)}$, and the exfoliated and annealed $\text{MoS}_{2x}\text{Se}_{2(1-x)}$ nanosheets. c) High-resolution XPS S 2p spectrum of bulk crystal of $\text{MoS}_{2x}\text{Se}_{2(1-x)}$, and the exfoliated and annealed $\text{MoS}_{2x}\text{Se}_{2(1-x)}$ nanosheets. d) UV-vis spectra of exfoliated and annealed $\text{MoS}_{2x}\text{Se}_{2(1-x)}$ nanosheet films on glass.

of ≈ 0.272 nm (Figure 3f), assignable to the (100) planes of the $\text{Mo}_x\text{W}_{1-x}\text{S}_2$ crystal. The EDS spectrum of a typical $\text{Mo}_x\text{W}_{1-x}\text{S}_2$ nanosheet gives strong signals of Mo, W, and S (Figure S9, Supporting Information) and these elements are homogeneously distributed in the ternary nanosheet (Figure S10, Supporting Information).

Moreover, the STEM was used to visualize the distribution of Mo and W atoms in the single-layer $\text{Mo}_x\text{W}_{1-x}\text{S}_2$ nanosheet. The atomic STEM image shows that the W and Mo atoms are randomly distributed in the single-layer nanosheet, forming a hexagonal lattice arrangement. Due to the greater Z number of W atom, it shows brighter contrast than does the Mo atoms (Figure S11, Supporting Information). In addition, the XPS analyses of three $\text{Mo}_x\text{W}_{1-x}\text{S}_2$ samples give similar results with the three $\text{MoS}_{2x}\text{Se}_{2(1-x)}$ samples, respectively. The exfoliated $\text{Mo}_x\text{W}_{1-x}\text{S}_2$ nanosheets show obvious shift to lower binding energy in comparison with the 2H bulk crystal in the Mo 3d, S 2p, and W 4f spectra, and the quenching of the 1T phase peaks can be observed after annealing (Figure 3g–i). The calculated concentration of metallic 1T phase is also as high as $\approx 66\%$ for the exfoliated $\text{Mo}_x\text{W}_{1-x}\text{S}_2$ based on the Mo 3d spectrum (Figure 3g). Similarly, all the three $\text{Mo}_x\text{W}_{1-x}\text{S}_2$ samples show three prominent peaks at 407, 380, and 357 cm^{-1} (Figure S12, Supporting

Information), corresponding to the MoS_2 -like A_{1g} , E_{2g}^1 , and WS_2 -like E_{2g}^1 modes of 2H $\text{Mo}_x\text{W}_{1-x}\text{S}_2$, respectively.^[41] The distorted 1T phase Raman active modes (J_1 : 150 cm^{-1} and J_2 : 215 cm^{-1}) in the lower frequency region can be observed in the exfoliated $\text{Mo}_x\text{W}_{1-x}\text{S}_2$ nanosheets (Figure S12, Supporting Information).^[33] The UV-vis absorption spectra give similar results to the $\text{MoS}_{2x}\text{Se}_{2(1-x)}$ nanosheet films, revealing the metallic 1T phase in the exfoliated $\text{Mo}_x\text{W}_{1-x}\text{S}_2$ nanosheets and the restoration of 2H phase after the exfoliated $\text{Mo}_x\text{W}_{1-x}\text{S}_2$ nanosheets were annealed at $300\text{ }^\circ\text{C}$ (Figure S13, Supporting Information).

As known, the single-layer MoS_2 nanosheets with high concentration of metallic 1T phase were prepared by exfoliating its bulk crystal via our Li-intercalation and exfoliation method.^[37] The detail characterizations of bulk crystal of MoS_2 , and exfoliated and annealed MoS_2 nanosheets by SEM, AFM, TEM, XPS, Raman spectroscopy, and UV-vis spectroscopy are shown in Figures S14–S18 (Supporting Information). All these results indicate that the exfoliated MoS_2 nanosheets also contain a high concentration of metallic 1T phase ($\approx 67\%$) (Figure S15a, Supporting Information). It proved the coexistence of 2H and 1T phases in the single-layer MoS_2 nanosheets.^[42] In this work, we have successfully used our electrochemical Li-intercalation and exfoliation

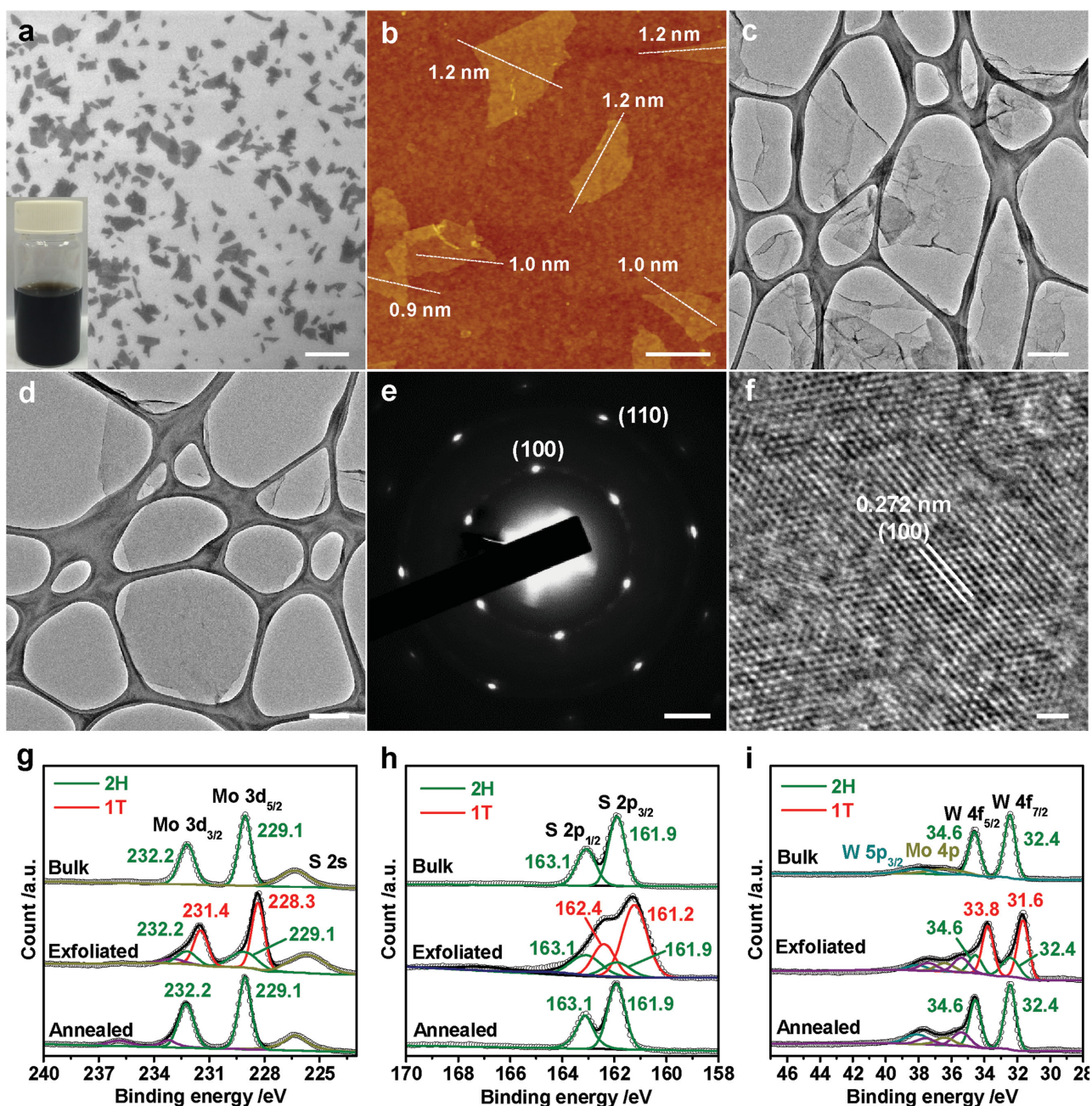


Figure 3. Characterization of $\text{Mo}_x\text{W}_{1-x}\text{S}_2$ nanosheets. a) SEM image and b) AFM height image of $\text{Mo}_x\text{W}_{1-x}\text{S}_2$ nanosheets (scale bars, a): 2 μm ; b): 500 nm). Inset in (a): photograph of the colloidal suspension of $\text{Mo}_x\text{W}_{1-x}\text{S}_2$ nanosheets. c) TEM image of $\text{Mo}_x\text{W}_{1-x}\text{S}_2$ nanosheets (scale bar, 500 nm). d) TEM image of a typical $\text{Mo}_x\text{W}_{1-x}\text{S}_2$ nanosheet (scale bar, 400 nm). e) The corresponding SAED pattern of the $\text{Mo}_x\text{W}_{1-x}\text{S}_2$ nanosheet in (d) (scale bar, 2 $1/\text{nm}$). f) HRTEM image of a typical $\text{Mo}_x\text{W}_{1-x}\text{S}_2$ nanosheet (scale bar, 1 nm). g) High-resolution Mo 3d XPS spectra of bulk crystal of $\text{Mo}_x\text{W}_{1-x}\text{S}_2$, and the exfoliated and annealed $\text{Mo}_x\text{W}_{1-x}\text{S}_2$ nanosheets. h) High-resolution S 2p XPS spectra of bulk crystal of $\text{Mo}_x\text{W}_{1-x}\text{S}_2$, and the exfoliated and annealed $\text{Mo}_x\text{W}_{1-x}\text{S}_2$ nanosheets. i) XPS high-resolution W 4f spectra of bulk crystal of $\text{Mo}_x\text{W}_{1-x}\text{S}_2$, and exfoliated and annealed $\text{Mo}_x\text{W}_{1-x}\text{S}_2$ nanosheets.

method to prepare single-layer ternary TMD nanosheets with high concentration of metallic 1T phase with the layered 2H-phase bulk crystals as the source. The phase transformation from the semiconducting 2H phase to metallic 1T phase occurs during the electrochemical Li-intercalation. Alternatively, in the previously reported intercalation of TMD bulk materials with n-butyllithium,^[26,33] it is believed that the electron transfer from the butyl to TMDs occurs, which destabilizes the pristine 2H phase and thus to induce the phase

transformation from 2H phase to metallic 1T phase.^[26,33] However, in our study, the electrons can be donated from the Li foil to TMD crystals (i.e., MoS_2 , $\text{MoS}_{2x}\text{Se}_{2(1-x)}$, and $\text{Mo}_x\text{W}_{1-x}\text{S}_2$) during the discharge process (Scheme 1),^[43,44] thus leading to the phase transformation to obtain TMD nanosheets with high-concentration metallic 1T phase. We believe that our method can also be used to effectively exfoliate other TMD materials and induce the phase transformation in the obtained single- or few-layer TMD nanosheets.

As known, TMD nanomaterials, such as MoS_2 and WS_2 particles^[45] and few-layer MoSe_2 nanosheets,^[46] can be used as cost-effective electrocatalysts in the CEs of DSSCs, which show good photovoltaic performance. Here, as a proof-of-concept application, a thin film of single-layer $\text{MoS}_{2x}\text{Se}_{2(1-x)}$ nanosheets with $\approx 66\%$ of metallic 1T phase drop-casted on an FTO substrate was used as the electrocatalyst for the triiodide reduction in I^-/I_3^- redox electrolyte in a DSSC, which exhibits higher electrocatalytic activity compared with the thin films of 2H-phase single-layer $\text{MoS}_{2x}\text{Se}_{2(1-x)}$ nanosheets and the single-layer MoS_2 nanosheets with $\approx 67\%$ of metallic 1T phase. In a typical experiment, the exfoliated single-layer $\text{MoS}_{2x}\text{Se}_{2(1-x)}$ nanosheet coated on an FTO substrate, referred to as FTO-exfoliated- $\text{MoS}_{2x}\text{Se}_{2(1-x)}$, by simple drop-casting method was used as the CE in a DSSC, in which an N719 dye-sensitized mesoporous TiO_2 electrode was used as the photoanode.^[47] The schematic illustration of DSSC device is shown in **Figure 4a**. The deposited $\text{MoS}_{2x}\text{Se}_{2(1-x)}$ nanosheet film has a thickness of ≈ 50 nm (Figure S19, Supporting Information). The 2H-phase $\text{MoS}_{2x}\text{Se}_{2(1-x)}$ nanosheet film on FTO, referred to as FTO-Annealed- $\text{MoS}_{2x}\text{Se}_{2(1-x)}$, was obtained by annealing the FTO-exfoliated- $\text{MoS}_{2x}\text{Se}_{2(1-x)}$ under Ar atmosphere at 300°C for 1 h. Figure 4b illustrates the photocurrent density–voltage (J – V) characteristic curves of DSSCs with three different CEs. The detailed photovoltaic parameters are summarized in **Table 1**. In a control experiment, the DSSC using the Pt-decorated FTO, referred to as

FTO-Pt, as CE has an open-circuit voltage (V_{oc}) of 0.80 V, short-circuit current density (J_{sc}) of 12.82 mA cm^{-2} , fill factor (FF) of 0.69, and power conversion efficiency (PCE) of 7.0%. When the FTO-exfoliated- $\text{MoS}_{2x}\text{Se}_{2(1-x)}$ was used as CE, the photovoltaic parameters, V_{oc} , J_{sc} , FF, and PCE are 0.75 V, 13.40 mA cm^{-2} , 0.65, and 6.5%, respectively. Although the FTO-Pt CE exhibits a little higher V_{oc} and FF, the FTO-exfoliated- $\text{MoS}_{2x}\text{Se}_{2(1-x)}$ gives a little higher J_{sc} . Therefore, their photovoltaic performance is comparable. In contrast, when the FTO-Annealed- $\text{MoS}_{2x}\text{Se}_{2(1-x)}$ was used as CE, the PCE is only 5.4% with $V_{\text{oc}} = 0.76\text{ V}$, $J_{\text{sc}} = 13.52\text{ mA cm}^{-2}$, and $\text{FF} = 0.52$. Although the changes of V_{oc} and J_{sc} are quite small, its FF shows a notable decrease compared with the other two CEs. For comparison, the photovoltaic performance of exfoliated MoS_2 nanosheets with $\approx 67\%$ of metallic 1T phase and annealed MoS_2 nanosheets with 2H phase deposited on FTO electrodes, referred to as FTO-exfoliated- MoS_2 and FTO-Annealed- MoS_2 , respectively, were also measured. Note that the MoS_2 nanosheet thin film has the similar thickness with the $\text{MoS}_{2x}\text{Se}_{2(1-x)}$ nanosheet thin film based on the preparation method (see the Experimental Section in the Supporting Information for details). Similarly, the FTO-exfoliated- MoS_2 also gives a higher FF (0.65) and PEC (6.0%) compared with the FTO-Annealed- MoS_2 ($\text{FF} = 0.58$ and $\text{PCE} = 5.1\%$) (Figure S20 and Table S1, Supporting Information). Based on the aforementioned results, both of the exfoliated $\text{MoS}_{2x}\text{Se}_{2(1-x)}$ and MoS_2 nanosheets with high concentration

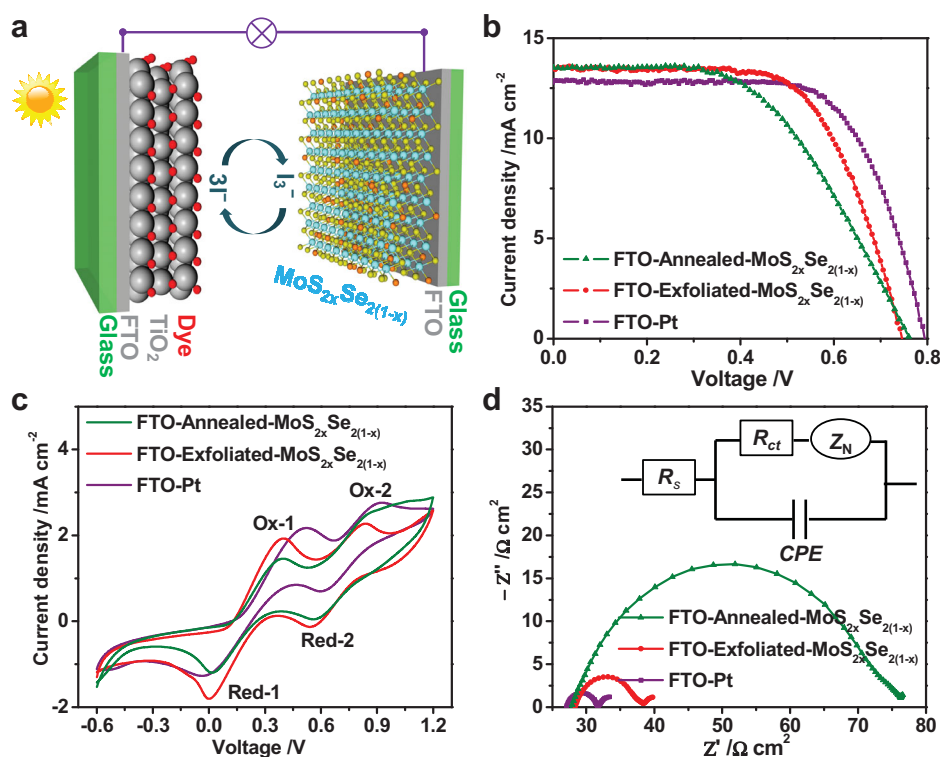


Figure 4. DSSCs based on $\text{MoS}_{2x}\text{Se}_{2(1-x)}$ nanosheets. a) Schematic illustration of a typical assembled DSSC with N719 dye-sensitized TiO_2 photoanode and FTO-exfoliated- $\text{MoS}_{2x}\text{Se}_{2(1-x)}$ CEs. b) J – V curves of DSSCs with FTO-exfoliated- $\text{MoS}_{2x}\text{Se}_{2(1-x)}$, FTO-Annealed- $\text{MoS}_{2x}\text{Se}_{2(1-x)}$, and FTO-Pt used as CEs measured under simulated sunlight 100 mW cm^{-2} (AM 1.5). c) CV curves of FTO-exfoliated- $\text{MoS}_{2x}\text{Se}_{2(1-x)}$, FTO-Annealed- $\text{MoS}_{2x}\text{Se}_{2(1-x)}$ and FTO-Pt CEs in the acetonitrile solution containing 10 mM of LiI , 1 mM of I_2 , and 0.1 M of LiClO_4 (supporting electrolyte). d) Nyquist plots of a symmetric dummy cell with configuration of two identical FTO-exfoliated- $\text{MoS}_{2x}\text{Se}_{2(1-x)}$, FTO-Annealed- $\text{MoS}_{2x}\text{Se}_{2(1-x)}$, or FTO-Pt electrodes (inset: a fitting equivalent circuit).

Table 1. Photovoltaic parameters of DSSCs with different counter electrodes and simulated data from the fitted EIS curves.

Counter electrode	V_{oc} [V]	J_{sc} [mA cm ⁻²]	FF [%]	PCE [%]	R_s [Ω cm ²]	R_{ct} [Ω cm ²]
FTO-Pt	0.80	12.82	0.69	7.0	27.07	2.28
FTO-exfoliated-MoS _{2x} Se _{2(1-x)}	0.75	13.40	0.65	6.5	28.40	4.60
FTO-Annealed-MoS _{2x} Se _{2(1-x)}	0.76	13.52	0.52	5.4	27.92	23.25

of 1T phase display better photovoltaic performance compared with the 2H ones after annealing.

The higher photovoltaic performance of exfoliated MoS_{2x}Se_{2(1-x)} should be ascribed to its higher electrocatalytic activity toward the tri-iodide reduction in comparison with the annealed one, which is supported by the cyclic voltammetry (CV) and electrochemical impedance spectroscopy (EIS). The CV curves in Figure 4c give two typical pairs of redox peaks for both FTO-exfoliated-MoS_{2x}Se_{2(1-x)} and FTO-Pt CEs, indicating the Pt-like electrocatalytic activity of exfoliated MoS_{2x}Se_{2(1-x)} nanosheets in the tri-iodide reduction. The two peaks correspond to the two-step reversible redox reaction in the I⁻/I₃⁻ electrolyte solution, i.e., the left pair (Ox-1 and Red-1): I₃⁻ + 2e⁻ ↔ 3I⁻, and the right pair (Ox-2 and Red-2): 3I₂ + 2e⁻ ↔ 2I₃⁻. However, one of the anodic peaks (Ox-2) could not be observed in the FTO-Annealed-MoS_{2x}Se_{2(1-x)} CE. Moreover, the cathodic peak density of Red-1 in FTO-exfoliated-MoS_{2x}Se_{2(1-x)} is higher than that of the FTO-Annealed-MoS_{2x}Se_{2(1-x)}, suggesting a faster redox reaction on FTO-exfoliated-MoS_{2x}Se_{2(1-x)} CE.^[48] Therefore, from the CV analysis, the FTO-exfoliated-MoS_{2x}Se_{2(1-x)} CE exhibits better electrocatalytic activity compared with FTO-Annealed-MoS_{2x}Se_{2(1-x)} CE. Similarly, the CV curves of FTO-exfoliated-MoS₂ and FTO-Annealed-MoS₂ CEs were also obtained and compared in Figure S19a (Supporting Information), further demonstrating the higher electrocatalytic activity of the exfoliated nanosheets compared with the one after annealing.

Furthermore, the electron transport process at the CE/electrolyte interface was studied by the EIS measurement in a symmetric dummy cell consisting of two identical CEs. Figure 4d shows the Nyquist plots for the MoS_{2x}Se_{2(1-x)} samples obtained in the dark without bias potential, which are fitted with the equivalent circuit (inset in Figure 4d).^[49] The semicircle in the high-frequency region presents the charge transfer resistance (R_{ct}) and the corresponding constant phase angle element at the CE/electrolyte interface. The arch in the low-frequency region indicates the diffusion resistance (Z_N) of the redox couple in the electrolyte. The intercept on the real axis is defined as the ohmic series resistance (R_s). In these parameters, R_{ct} and R_s are highly related to the electrocatalytic activity of CEs for the tri-iodide reduction. The obtained R_{ct} and R_s for two MoS_{2x}Se_{2(1-x)} CEs are summarized in Table 1. Obviously, the FTO-Annealed-MoS_{2x}Se_{2(1-x)} has a slightly lower R_s (27.92 Ω cm²) compared with the FTO-exfoliated-MoS_{2x}Se_{2(1-x)} (28.40 Ω cm²), which might arise from the enhanced adhesion between the electrocatalyst layer (i.e., MoS_{2x}Se_{2(1-x)} film) and the FTO substrate after the thermal annealing.^[49] However, compared with

FTO-Annealed-MoS_{2x}Se_{2(1-x)} with R_{ct} of 23.25 Ω cm², the FTO-exfoliated-MoS_{2x}Se_{2(1-x)} gives much lower R_{ct} (4.60 Ω cm²), close to that of FTO-Pt CE (2.28 Ω cm²), suggesting its higher electrocatalytic activity. Based on the previous report on the equivalent circuit model for DSSCs,^[50] the FF is inversely proportional to the sum of R_s and R_{ct} . Due to the small difference of R_s for FTO-exfoliated-MoS_{2x}Se_{2(1-x)} and FTO-Annealed-MoS_{2x}Se_{2(1-x)}, the higher R_{ct} (23.25 Ω cm²) contributes to the lower FF of FTO-Annealed-MoS_{2x}Se_{2(1-x)}. As known, the higher R_{ct} may be ascribed to the lower conductivity of the semiconducting 2H-phase MoS_{2x}Se_{2(1-x)} after annealing of the exfoliated-MoS_{2x}Se_{2(1-x)},²⁵ which induces the sluggish electron transfer process. In contrast, the high concentration of metallic 1T phase in the FTO-exfoliated-MoS_{2x}Se_{2(1-x)} (\approx 66%) renders its higher conductivity, which can facilitate the electron transport from the CE surface to the redox electrolyte for the tri-iodide reduction. Similarly, the FTO-exfoliated-MoS₂ also gives a higher FF (0.65) because of its much lower R_{ct} (19.60 Ω cm²) compared with the FTO-Annealed-MoS₂ (FF = 0.58 and R_{ct} = 121.1 Ω cm²) (Figure S21a and Table S1, Supporting Information), indicating the higher electrocatalytic activity of the exfoliated MoS₂ nanosheets compared with those after annealing. Impressively, the FTO-exfoliated-MoS_{2x}Se_{2(1-x)} gives R_{ct} of 4.60 Ω cm², much lower than that of the FTO-exfoliated-MoS₂ with R_{ct} of 19.60 Ω cm² (Figure S21b, Supporting Information). The much lower R_{ct} of exfoliated MoS_{2x}Se_{2(1-x)} compared with the exfoliated MoS₂ with similar concentration of 1T phase can be ascribed to higher conductivity induced by Se doping (Figure S21b, Supporting Information),^[51] resulting in its higher catalytic activity toward the tri-iodide reduction. Therefore, when integrated in a DSSC device, the FTO-exfoliated-MoS_{2x}Se_{2(1-x)} gives a higher PEC (6.5%) than does FTO-exfoliated-MoS₂ (6.0%).

Based on all the aforementioned discussion, we uncover that the FTO-exfoliated-MoS_{2x}Se_{2(1-x)} gives higher electrocatalytic activity toward the tri-iodide reduction compared with the FTO-exfoliated-MoS₂ and FTO-Annealed-MoS_{2x}Se_{2(1-x)}. Therefore, when used as a CE in DSSC and compared with other nanosheets investigated in this study, the FTO-exfoliated-MoS_{2x}Se_{2(1-x)} exhibits the best photovoltaic performance (PCE = 6.5%), little lower than that of FTO-Pt (PCE = 7.0%). The summary and comparison of photovoltaic performance of TMD materials as CEs in DSSCs are shown in Table S2 (Supporting Information). Considering the high-performance device is incorporated with the nanosheet film deposited by simple drop-casting method at room temperature, the as-prepared nanosheets can be coated on flexible substrates to construct flexible photovoltaic devices in the near future.

In summary, single-layer ternary TMD nanosheets with high concentration of metallic 1T phase, including MoS_{2x}Se_{2(1-x)} and Mo_xW_{1-x}S₂, have been prepared in high-yield and large amount from their 2H-phase layered bulk crystals via our recently developed electrochemical Li-intercalation and exfoliation method. To the best of our knowledge, it is the first time to realize the preparation of single-layer ternary TMD nanosheets with high concentration of metallic 1T phase (\approx 66%) at high-yield and large scale. The exfoliated ternary

MoS_{2-x}Se_{2(1-x)} nanosheets can be easily coated on an FTO to form a thin film by simple drop-coating method, and then directly used as an efficient electrocatalyst for the tri-iodide reduction on the CE in a DSSC. It showed a PCE of 6.5%, which is higher than that of the annealed MoS_{2-x}Se_{2(1-x)} (5.4%) and exfoliated MoS₂ (6.0%). The facile, highly efficient, scalable production of single-layer MoS_{2-x}Se_{2(1-x)} nanosheets with high concentration of metallic 1T phase make it a promising electrocatalyst for fabrication of high-performance Pt-free DSSCs. Moreover, this nanosheet could also be promising for other applications including the electrocatalytic hydrogen evolution, supercapacitors, and electrochemical sensors.

Supporting Information

Supporting Information is available from the Wiley Online Library or from the author.

Acknowledgements

C.L.T., W.Z., and A.C. contributed equally to this work. This work was supported by MOE under AcRF Tier 2 (ARC 26/13, No. MOE2013-T2-1-034; ARC 19/15, No. MOE2014-T2-2-093) and AcRF Tier 1 (RGT18/13, RG5/13), and NTU under Start-Up Grant (M4081296.070.500000) in Singapore. This research is also conducted by NTU-HUJ-BGU Nanomaterials for Energy and Water Management Programme under the Campus for Research Excellence and Technological Enterprise (CREATE) that is supported by the National Research Foundation, Prime Minister's Office, Singapore. Z.F. and C.H.J. acknowledge the financial support by the National Basic Research Program of China (Grants No. 2014CB932500 and No. 2015CB921000) and the National Science Foundation of China (Grants No. 51222202 and No. 51472215). This work made use of the resources of the Center of Electron Microscopy of Zhejiang University. The experiments performed at the Molecular Foundry, Lawrence Berkeley National Laboratory were supported by the U.S. Department of Energy under contract no. DE-AC02-05CH11231.

- [1] Q. H. Wang, K. Kalantar-Zadeh, A. Kis, J. N. Coleman, M. S. Strano, *Nat. Nanotechnol.* **2012**, *11*, 699.
- [2] X. Huang, Z. Y. Zeng, H. Zhang, *Chem. Soc. Rev.* **2013**, *42*, 1934.
- [3] H. Zhang, *ACS Nano* **2015**, *9*, 9451.
- [4] C. L. Tan, H. Zhang, *Chem. Soc. Rev.* **2015**, *44*, 2713.
- [5] C. L. Tan, H. Zhang, *J. Am. Chem. Soc.* **2015**, *137*, 12162.
- [6] B. Radisavljevic, A. Radenovic, J. Brivio, V. Giacometti, A. Kis, *Nat. Nanotechnol.* **2011**, *6*, 147.
- [7] Z. Y. Yin, H. Li, H. Li, L. Jiang, Y. M. Shi, Y. H. Sun, G. Lu, Q. Zhang, X. D. Chen, H. Zhang, *ACS Nano* **2012**, *6*, 74.
- [8] J. F. Xie, J. J. Zhang, S. Li, F. Grote, X. D. Zhang, H. Zhang, R. X. Wang, Y. Lei, B. C. Pan, Y. Xie, *J. Am. Chem. Soc.* **2013**, *135*, 17881.
- [9] L. Cheng, W. Huang, Q. Gong, C. Liu, Z. Liu, Y. Li, H. Dai, *Angew. Chem. Int. Ed.* **2014**, *53*, 7860.
- [10] C. F. Zhu, Z. Y. Zeng, H. Li, F. Li, C. H. Fan, H. Zhang, *J. Am. Chem. Soc.* **2013**, *135*, 5998.
- [11] F. K. Perkins, A. L. Friedman, E. Cobas, P. M. Campbell, G. G. Jernigan, B. T. Jonker, *Nano Lett.* **2013**, *13*, 668.
- [12] C. L. Tan, P. Yu, Y. L. Hu, J. Z. Chen, Y. Huang, Y. Q. Cai, Z. M. Luo, B. Li, Q. P. Lu, L. H. Wang, Z. Liu, H. Zhang, *J. Am. Chem. Soc.* **2015**, *137*, 10430.
- [13] Y. F. Sun, S. Gao, Y. Xie, *Chem. Soc. Rev.* **2014**, *43*, 530.
- [14] G. Du, Z. Guo, S. Wang, R. Zeng, Z. Chen, H. Liu, *Chem. Commun.* **2010**, *46*, 1106.
- [15] L. Cheng, J. J. Liu, X. Gu, H. Gong, X. Z. Shi, T. Liu, C. Wang, X. Y. Wang, G. Liu, H. Y. Xing, W. B. Bu, B. Q. Sun, Z. Liu, *Adv. Mater.* **2014**, *26*, 1886.
- [16] Y. Chen, C. L. Tan, H. Zhang, L. Z. Wang, *Chem. Soc. Rev.* **2015**, *44*, 2681.
- [17] D. O. Dumcenco, H. Kobayashi, Z. Liu, Y. S. Huang, K. Suenaga, *Nat. Commun.* **2013**, *4*, 1351.
- [18] Y. F. Chen, J. Y. Xi, D. O. Dumcenco, Z. Liu, K. Suenaga, D. Wang, Z. G. Shuai, Y. S. Huang, L. M. Xie, *ACS Nano* **2013**, *7*, 4610.
- [19] Y. J. Gong, Z. Liu, A. R. Lupini, G. Shi, J. H. Lin, S. Najmaei, Z. Lin, A. L. Elías, A. Berkdemir, G. You, H. Terrones, M. Terrones, R. Vajtai, S. T. Pantelides, S. J. Pennycook, J. Lou, W. Zhou, P. M. Ajayan, *Nano Lett.* **2014**, *14*, 442.
- [20] H. L. Li, X. D. Duan, X. P. Wu, X. J. Zhuang, H. Zhou, Q. L. Zhang, X. L. Zhu, W. Hu, P. Y. Ren, P. F. Guo, L. Ma, X. P. Fan, X. X. Wang, J. Y. Xu, A. L. Pan, X. F. Duan, *J. Am. Chem. Soc.* **2014**, *136*, 3756.
- [21] J. Mann, Q. Ma, P. M. Odenthal, M. Isarraraz, D. Le, E. Preciado, D. Barroso, K. Yamaguchi, G. von Son Palacio, A. Nguyen, T. Tran, M. Wurch, A. Nguyen, V. Klee, S. Bobek, D. Z. Sun, T. F. Heinz, T. S. Rahman, R. Kawakami, L. Bartels, *Adv. Mater.* **2014**, *26*, 1399.
- [22] Q. L. Feng, Y. M. Zhu, J. H. Hong, M. Zhang, W. J. Duan, N. N. Mao, J. X. Wu, H. Xu, F. L. Dong, F. Lin, C. H. Jin, C. M. Wang, J. Zhang, L. M. Xie, *Adv. Mater.* **2014**, *26*, 2648.
- [23] V. Kiran, D. Mukherjee, R. N. Jenjeti, S. Sampath, *Nanoscale* **2014**, *6*, 12856.
- [24] K. Funaki, K. Tezuka, Y. Shan, *J. Phys. Status Solidi A* **2014**, *211*, 901.
- [25] Q. F. Gong, L. Cheng, C. L. Liu, M. Zhang, Q. L. Feng, H. L. Ye, M. Zeng, L. M. Xie, Z. Liu, Y. G. Li, *ACS Catal.* **2015**, *5*, 2213.
- [26] D. Voiry, A. Mohite, M. Chhowalla, *Chem. Soc. Rev.* **2015**, *44*, 2702.
- [27] D. Voiry, H. Yamaguchi, J. Li, R. Silva, D. C. B. Alves, T. Fujita, M. Chen, T. Asefa, V. B. Shenoy, G. Eda, M. Chhowalla, *Nat. Mater.* **2013**, *12*, 850.
- [28] D. M. Voiry, A. M. Salehi, R. Silva, T. Fujita, M. Chen, T. Asefa, V. B. Shenoy, G. Eda, M. Chhowalla, *Nano Lett.* **2013**, *13*, 6222.
- [29] M. Lukowski, A. S. Daniel, F. Meng, A. Forticaux, L. Li, S. Jin, *J. Am. Chem. Soc.* **2013**, *135*, 10274.
- [30] M. Acerce, D. Voiry, M. Chhowalla, *Nat. Nanotechnol.* **2015**, *10*, 313.
- [31] R. Kappera, D. Voiry, S. E. Yalcin, B. Branch, G. Gupta, A. D. Mohite, M. Chhowalla, *Nat. Mater.* **2014**, *13*, 1128.
- [32] S. Cho, S. Kim, J. H. Kim, J. Zhao, J. Seok, D. H. Keum, J. Baik, D.-H. Choe, K. J. Chang, K. Suenaga, S. W. Kim, Y. H. Lee, H. Yang, *Science* **2015**, *349*, 625.
- [33] G. Eda, H. Yamaguchi, D. Voiry, T. Fujita, M. Chen, M. Chhowalla, *Nano Lett.* **2011**, *11*, 5111.
- [34] Y.-C. Lin, D. O. Dumcenco, Y.-S. Huang, K. Suenaga, *Nat. Nanotechnol.* **2014**, *9*, 391.
- [35] Y. Yu, F. Yang, X. F. Lu, Y. J. Yan, Y.-H. Cho, L. Ma, X. Niu, S. Kim, Y.-W. Son, D. Feng, S. Li, S.-W. Cheong, X. H. Chen, Y. Zhang, *Nat. Nanotechnol.* **2015**, *10*, 270.
- [36] B. Mahler, V. Hoepfner, K. Liao, G. A. Ozin, *J. Am. Chem. Soc.* **2014**, *136*, 14121.
- [37] Z. Y. Zeng, Z. Y. Yin, X. Huang, H. Li, Q. Y. He, G. Lu, F. Boey, H. Zhang, *Angew. Chem. Int. Ed.* **2011**, *50*, 11093.
- [38] M. A. Baker, R. Gilmore, C. Lenardi, W. Gissler, *Appl. Surf. Sci.* **1999**, *150*, 255.

- [39] A. Mallouky, J. C. Bernede, *Thin Solid Films* **1988**, *158*, 285.
- [40] S. H. Su, Y. T. Hsu, Y. H. Chang, M. H. Chiu, C. L. Hsu, W. T. Hsu, W. H. Chang, J. H. He, L. J. Li, *Small* **2014**, *10*, 2589.
- [41] Y. F. Chen, D. O. Dumcenco, Y. M. Zhu, X. Zhang, N. N. Mao, Q. L. Feng, M. Zhang, J. Zhang, P. H. Tan, Y. S. Huang, L. M. Xie, *Nanoscale* **2014**, *6*, 2833.
- [42] X. Huang, Z. Y. Zeng, S. Y. Bao, M. F. Wang, X. Y. Qi, Z. X. Fan, H. Zhang, *Nat. Commun.* **2013**, *4*, 1444.
- [43] M. A. Py, R. R. Haering, *Can. J. Phys.* **1983**, *61*, 76.
- [44] H. Wang, Z. Lu, S. Xu, D. Kong, J. J. Cha, G. Zheng, P.-C. Hsu, K. Yan, D. Bradshaw, F. B. Prinz, Y. Cui, *Proc. Natl. Acad. Sci. USA* **2013**, *110*, 19701.
- [45] M. X. Wu, Y. D. Wang, X. Lin, N. S. Yu, L. Wang, L. L. Wang, A. Hagfeldt, T. L. Ma, *Phys. Chem. Chem. Phys.* **2011**, *13*, 19298.
- [46] H. J. Chen, Y. A. Xie, H. L. Cui, W. Zhao, X. L. Zhu, Y. M. Wang, X. J. Lü, F. Q. Huang, *Chem. Commun.* **2014**, *50*, 4475.
- [47] B. O'regan, M. Grätzel, *Nature* **1991**, *353*, 737.
- [48] H. Sun, Y. Luo, Y. Zhang, D. Li, Z. Yu, K. Li, Q. Meng, *J. Phys. Chem. C* **2010**, *114*, 11673.
- [49] M. Wu, X. Lin, A. Hagfeldt, T. Ma, *Angew. Chem. Int. Ed.* **2011**, *50*, 3520.
- [50] N. Koide, A. Islam, Y. Chiba, L. Han, *J. Photoch. Photobiol. A* **2006**, *182*, 296.
- [51] X. Ren, Q. Ma, H. Fan, L. Pang, Y. Zhang, Y. Yao, X. Ren, S. Liu, *Chem. Commun.* **2015**, *51*, 15997.

Received: January 3, 2016
Revised: January 31, 2016
Published online: February 24, 2016